J. Fluid Mech. (2021), *vol*. 911, A11, doi:10.1017/jfm.2020.1040

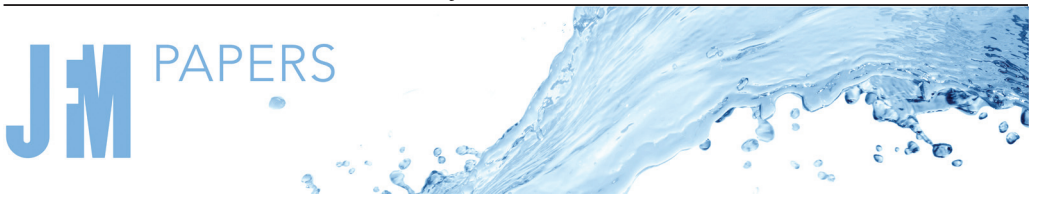

Structure and rheology of suspensions of spherical strain-hardening capsules

Othmane Aouane[1],†, Andrea Scagliarini[2,3] and Jens Harting[1,4]

[1]Helmholtz Institute Erlangen-Nürnberg for Renewable Energy, Forschungszentrum Jülich, Fürther Straße 248, 90429 Nürnberg, Germany

[2]Istituto per le Applicazioni del Calcolo 'M. Picone', IAC-CNR, Via dei Taurini 19, 00185 Roma, Italy

[3]INFN, sezione Roma "Tor Vergata", via della Ricerca Scientifica 1, 00133 Rome, Italy

[4]Department of Chemical and Biological Engineering and Department of Physics, Friedrich-Alexander-Universität Erlangen-Nürnberg, Fürther Straße 248, 90429 Nürnberg, Germany

(Received 9 March 2020; revised 13 August 2020; accepted 17 November 2020)

We investigate the rheology of strain-hardening spherical capsules, from the dilute to the concentrated regime under a confined shear flow using three-dimensional numerical simulations. We consider the effect of capillary number, volume fraction and membrane inextensibility on the particle deformation and on the effective suspension viscosity and normal stress differences of the suspension. The suspension displays a shear-thinning behaviour that is a characteristic of soft particles such as emulsion droplets, vesicles, strain-softening capsules and red blood cells. We find that the membrane inextensibility plays a significant role on the rheology and can almost suppress the shear-thinning. For concentrated suspensions a non-monotonic dependence of the normal stress differences on the membrane inextensibility is observed, reflecting a similar behaviour in the particle shape. The effective suspension viscosity, instead, grows and eventually saturates, for very large inextensibilities, approaching the solid particle limit. In essence, our results reveal that strain-hardening capsules share rheological features with both soft and solid particles depending on the ratio of the area dilatation to shear elastic modulus. Furthermore, the suspension viscosity exhibits a universal behaviour for the parameter space defined by the capillary number and the membrane inextensibility, when introducing the particle geometrical changes at the steady state in the definition of the volume fraction.

Key words: capsule/cell dynamics, suspensions, rheology

† Email address for correspondence: o.aouane@fz-juelich.de

1. Introduction

Capsules are closed elastic polymeric membranes, formed by cross-linking proteins to polysaccharides, and encapsulating a liquid droplet core (Lévy & Edwards-Lévy 1996; Edwards-Lévy & Lévy 1999). Their typical diameter spans from a few nanometres to a few millimetres. Capsules are primarily used as controlled delivery systems of active substances with practical applications gearing around pharmaceutical industry (Donbrow 1991; De Cock *et al.* 2010), food processing (Sagis *et al.* 2008), cosmetics (Miyazawa *et al.* 2000), household products such as paints (Suryanarayana, Rao & Kumar 2008), while showing promising applications and future perspectives in areas such as thermal energy storage (Sarı, Alkan & Karaipekli 2010), and injectable scaffolds for soft tissue regeneration (Munarin *et al.* 2010). The release mechanisms of the active agents cover time scales going from a few seconds to days and can occur either via capsule burst or through slow and prolonged diffusion (Neubauer, Poehlmann & Fery 2014). Capsules with a membrane made of polysiloxane will burst under continuous elongation (Walter, Rehage & Leonhard 2001; Koleva & Rehage 2012), similar to droplets, whereas membranes formed with pure human serum albumin (HSA) or HSA–alginate can sustain very large deformations without rupture (Carin *et al.* 2003; de Loubens *et al.* 2015) making them a good model for mimicking biological cells. The mechanical properties of the capsules can be probed by partial aspiration with a micropipette (Hochmuth 2000), atomic force microscopy (Fery & Weinkamer 2007), compression tests (Chang & Olbricht 1993*b*; Rachik *et al.* 2006) or in flow conditions by measuring the elongation of the particle and extracting the shear and area dilatation moduli using the appropriate hyperelastic constitutive law (de Loubens *et al.* 2015).

When subject to external stresses, capsules can exhibit a strain-softening or a strain-hardening behaviour depending on the composition and the fabrication protocol of their membrane. Those behaviours can be well recovered with hyperelastic constitutive laws such as the generalised Hooke, Mooney–Rivlin, neo-Hookean and Skalak laws (de Loubens *et al.* 2015; Barthès-Biesel 2016). The deformation and dynamics of a single capsule under different flow conditions have been thoroughly investigated by many authors: (i) numerically (Navot 1998; Ramanujan & Pozrikidis 1998; Lac *et al.* 2004; Li & Sarkar 2008; Bagchi & Kalluri 2009; Dodson & Dimitrakopoulos 2009; Farutin, Biben & Misbah 2014; Dupont *et al.* 2016; Boedec, Leonetti & Jaeger 2017), (ii) analytically (Barthès-Biesel 1980; Barthès-Biesel & Rallison 1981; Vlahovska *et al.* 2011) and (iii) experimentally (Chang & Olbricht 1993*a*,*b*; de Loubens *et al.* 2015, 2016; Häner, Heil & Juel 2020). Under a simple shear flow, initially non-spherical capsules can exhibit several complex dynamics including the steady and oscillating tank-treading, tumbling and swinging motions (also called vacillating-breathing in the literature). These dynamics are the result of the interplay between different parameters such as the capillary number, the confinement, and the viscosity contrast between the inner and the suspending fluids (Bagchi & Kalluri 2009; Vlahovska *et al.* 2011; Walter, Salsac & Barthès-Biesel 2011). Conversely, a spherical capsule exhibits only a steady tank-treading motion characterised by a fixed orientation angle with respect to the flow and a steady-state deformed shape while the membrane undergoes a tank-treading motion (Bagchi & Kalluri 2011; de Loubens *et al.* 2016).

Most end-use applications of capsules involve many particle interactions, and often different coupled time scales, with nonlinearity appearing already on the level of the single-particle mechanics. This level of complexity requires a numerical approach to understand the behaviour of suspensions of capsules, the correlation between their

microstructure and rheology, and how it compares with well-studied systems such as solid particles and emulsions of drops.

The rheology of a dilute suspension of rigid spheres in an unbounded shear flow has been addressed analytically in the original work of Einstein (1906, 1911) and extended to the second order by Batchelor & Green (1972) to include pair hydrodynamic interactions. Empirical, semi-empirical and analytical models were proposed in the literature to predict the change of the relative viscosity with the volume fraction of rigid sphere suspensions from the dilute to the concentrated regimes (Eilers 1941; Mooney 1951; Maron & Pierce 1956; Krieger & Dougherty 1959; Frankel & Acrivos 1967). Experiments and numerical simulations have revealed that a suspension of rigid particles exhibits shear-thinning, Newtonian and shear-thickening behaviour, respectively, as the shear rate is increased. Both normal stress differences, N_1 and N_2, have been reported to bear a negative sign with a larger magnitude for N_2 with respect to N_1. The sign of N_1 is still subject to discussions because its magnitude is very small. Numerical simulations performed by Sierou & Brady (2002) and Gallier *et al.* (2014, 2016) have pointed toward the possibility of two distinct physical origins of both normal stress differences. Here N_2 is associated with particle–particle collisions, whereas N_1 is mostly of hydrodynamic nature and is affected significantly by the presence or absence of boundaries. Detailed reviews on the rheology of solid particle suspensions can be found in Stickel & Powell (2005), Mueller, Llewellin & Mader (2010) and Guazzelli & Pouliquen (2018).

Non-Newtonian behaviour in the form of shear-thinning has been reported for emulsions of drops, strain-softening capsules and closed phospholipid bilayer membranes (vesicles). These three classes of deformable particles are characterised by a thin, continuous and impermeable interface encapsulating an internal fluid. However, the interface mechanical properties are different. They all exhibit a negative N_2 and a positive N_1, and unlike rigid particles, the magnitude of N_1 is larger than N_2, which most probably indicates a more dominant role of hydrodynamic interactions as compared with particle–particle collisions (Loewenberg & Hinch 1996; Clausen, Reasor & Aidun 2011; Vlahovska & Gracia 2007; Zhao & Shaqfeh 2013; Matsunaga *et al.* 2016). In analogy to drops, a capillary number, quantifying the shear elastic resistance of the membrane to external stresses, has been widely used in the literature of capsules regardless of the nature of the hyperelastic law and the number of moduli characterising the membrane mechanics. Bagchi & Kalluri (2010) have shown that for a single strain-hardening capsule under a simple shear flow, the ratio of the area dilatation to shear elastic moduli, characterising the local inextensibility of the membrane, leads to some atypical effects on the intrinsic viscosity and the shear-thinning behaviour. For a non-dilute suspension of anisotropic strain-hardening capsules, Gross, Krüger & Varnik (2014) have reported that for small capillary number the effect of the ratio of the area dilatation to shear elastic moduli on the suspension rheology is negligible.

This paper is devoted to study the dynamics of suspensions of model soft particles with a strain-hardening character, such as certain types of capsules (Carin *et al.* 2003), focusing on the role played by a material property of the membrane, namely its inextensibility, on the capsule deformation and on the suspension rheology, at varying the concentration of the dispersed phase and applied shear. To the best of the authors' knowledge the contribution of the local inextensibility of the membrane to the rheology of semi-dilute and concentrated suspensions of initially spherical strain-hardening capsules has so far not been studied.

The paper is organised as follows. We describe the numerical method in § 2 (benchmarks are provided in appendix A). We then present and discuss our numerical results for the dilute, semi-dilute and concentrated regimes as a function of the parameter C quantifying

the inextensibility of the membrane and the capillary number Ca in § 3. The concluding remarks and further discussions are given in § 4.

2. Numerical method

2.1. *Lattice Boltzmann method*

The Navier–Stokes equations are recovered in the limit of small Mach and Knudsen numbers by the lattice Boltzmann method (LBM), which is based on the discretisation of the Boltzmann–BGK (Bhatnagar, Gross & Krook 1954) equation in time and phase space (Benzi, Succi & Vergassola 1992; Succi 2001; Krüger *et al.* 2017). The LBM describes the evolution of the single-particle distribution function $f_i(\boldsymbol{x}, t)$ at a position $\boldsymbol{x}$ and time t with a microscopic velocity $\boldsymbol{c}_i$, where $i = 1 \ldots Q$, on a regular D-dimensional lattice in discrete time steps Δt. We consider in this work a $D3Q19$ model corresponding to a three-dimensional lattice with $Q = 19$ velocities. The lattice Boltzmann equation reads

$$f_i(\boldsymbol{x} + \boldsymbol{c}_i\Delta t, t + \Delta t) - f_i(\boldsymbol{x}, t) = \Omega_i(\boldsymbol{x}, t) + F_i(\boldsymbol{x}, t)\Delta t, \tag{2.1}$$

with

$$\Omega_i(\boldsymbol{x}, t) = -\frac{\Delta t}{\tau}[f_i(\boldsymbol{x}, t) - f_i^{eq}(\boldsymbol{x}, t)], \tag{2.2}$$

and

$$f_i^{eq}(\boldsymbol{x}, t) = \omega_i\rho\left[1 + \frac{(\boldsymbol{c}_i \cdot \boldsymbol{u})}{c_s^2} + \frac{1}{2}\frac{(\boldsymbol{c}_i \cdot \boldsymbol{u})^2}{c_s^4} - \frac{1}{2}\frac{|\boldsymbol{u}|^2}{c_s^2}\right], \tag{2.3}$$

where τ is a relaxation time related to the fluid dynamic viscosity by $\mu_0 = \rho_0 c_s^2(\tau - \Delta t/2)$ (ρ_0 being the mean fluid density). Here $c_s = (1/\sqrt{3})(\Delta x/\Delta t)$ denotes the lattice speed of sound, Δx is the lattice constant, ω_i are lattice weights and $f_i^{eq}(\boldsymbol{x}, t)$ is the equilibrium probability distribution function, depending on the fluid density ρ and velocity $\boldsymbol{u}$ fields as a truncated expansion of the Maxwell–Boltzmann distribution (valid at small Mach number, $Ma = |\boldsymbol{u}|/c_s \ll 0.1$). Here F_i on the right-hand side of (2.1) is a source term accounting for any external or internal force and will be used here to incorporate the forces exerted by the membrane on the fluid through the immersed boundary method (IBM). For a D3Q19 LBM, the lattice weights ω_i read as $1/3$, $1/18$ and $1/36$ for $i = 1$, $i = 2, \ldots, 7$ and $i = 8, \ldots, 19$, respectively. The macroscopic fluid density ρ and velocity $\boldsymbol{u}$ are deduced from the moments of the discrete probability distribution functions as

$$\rho = \sum_{i=1}^{19} f_i(\boldsymbol{x}, t) \quad \text{and} \quad \boldsymbol{u} = \sum_{i=1}^{19} f_i(\boldsymbol{x}, t)\boldsymbol{c}_i/\rho. \tag{2.4a,b}$$

For convenience, we set the lattice constant, the time step, the mean fluid density and the relaxation time to unity.

2.2. *Membrane model*

The capsule is modelled as a two-dimensional hyperelastic thin shell encapsulating an inner fluid and suspended in an outer fluid. The interior and exterior fluids are Newtonian with equal densities and viscosities. The surface of the capsule is discretised into a triangular mesh and endowed with a resistance to in-plane deformations. The membrane Lagrangian variables are defined on a moving curvilinear mesh with coordinates (ξ_1, ξ_2),

freely evolving on the Cartesian mesh on which lies the Eulerian fluid variables. We consider the case of a strain-hardening membrane using the hyperelastic law introduced by Skalak (1973), where the in-plane elastic deformations are governed by shear and area dilatation resistances. In terms of the deformation invariants, $I_1 = \lambda_1^2 + \lambda_2^2 - 2$ and $I_2 = \lambda_1^2\lambda_2^2 - 1$, where λ_1 and λ_2 are the principal stretching ratios on an element of the membrane surface, the strain energy over the surface of the capsule (Ω_S) reads as

$$E_s = \int_{\Omega_S} \frac{G_s}{4}[I_1^2 + 2I_1 - 2I_2 + CI_2^2]\,\mathrm{d}\Omega_S. \tag{2.5}$$

Here, G_s is the elastic shear modulus and C is a constant related to the strain-hardening character of the membrane through the scaled area dilatation modulus G_a such as $G_a/G_s = 1 + 2C$. In other words, increasing the value of C enhances the local inextensibility of the membrane (hereafter, we refer to C as membrane inextensibility) and makes the capsule more strain-hardening. In the small deformation limit, C and the surface Poisson ratio (ν_s) are related by $C = \nu_s/(1 - \nu_s)$ (see Barthès-Biesel, Diaz & Dhenin 2002). The elastic deformations on the surface of the particle are evaluated numerically using a linear finite element method following the approach described in Krüger, Varnik & Raabe (2011). In addition to shear elasticity and area dilatation, capsules may also exhibit a resistance to out-of-plane deformations (bending). The existence of a non-negligible bending energy depends on the protocol used to fabricate the capsule and the composition of the encapsulating membrane (de Loubens *et al.* 2014, 2015; Gubspun *et al.* 2016). Although it can be of interest to investigate the interplay between the bending and the shear elasticity under different flow conditions, we choose to focus, here, on the role of the area dilatation, which has been somehow overlooked in the existing literature, and we consider, thus, capsules without bending resistance. The volume of the capsules is prescribed using a penalty function that reads as

$$E_v = \frac{\kappa_v}{2}\frac{[V - V_0]^2}{V_0}, \tag{2.6}$$

where κ_v is a modulus that controls the deviation from the reference volume V_0 corresponding to the stress-free shape. The membrane force is calculated on each membrane node ($\boldsymbol{X}^m$) using the principle of virtual work, such that

$$\boldsymbol{F}^m = -\frac{\partial E(\boldsymbol{X}^m)}{\partial \boldsymbol{X}^m}, \tag{2.7}$$

where $E = E_s + E_v$ is the membrane total energy.

To avoid overlap between capsules in relatively dense systems, we introduce a short-range repulsive force intended to mimic the normal component of the lubrication force. The repulsive force acts when the distance between two nodes from different capsules is below the cut-off distance δ_0, which is set here to the minimum value of $1\Delta x$ corresponding to the fluid resolution limit of the LBM, and vanishes at a node-to-node distance $d_{ij} \geqslant \delta_0$. Its expression is given by

$$\boldsymbol{F}_{rep} = \begin{cases} \bar{\epsilon}\left[\left(\dfrac{\Delta x}{d_{ij}}\right)^2 - \left(\dfrac{\Delta x}{\delta_0}\right)^2\right]\dfrac{\boldsymbol{d}_{ij}}{d_{ij}} & \text{if } d_{ij} < \delta_0 \\ \boldsymbol{0} & \text{if } d_{ij} \geqslant \delta_0 \end{cases}, \tag{2.8}$$

where $\bar{\epsilon}$ is the interaction strength with the dimension of a force. Equation (2.8) was suggested by Glowinski *et al.* (2001) for suspension of rigid particles, and used by

Gross *et al.* (2014) to study the rheology of very dense suspensions of red blood cells in a shear flow. Other contact models based for example on an exponential repulsive force or a Lennard–Jones potential can also be used (Buxton *et al.* 2005; MacMeccan III 2007; Guckenberger & Gekle 2016). The effect of the short-range repulsive force on the rheology of strain-hardening capsules is discussed in appendix A.4.

2.3. *Membrane dynamics*

For the fluid–membrane coupling, we use the IBM (Peskin 2002). In the IBM the Lagrangian massless nodes are interacting with the Eulerian fluid nodes using an interpolation function in a two-way coupling scheme: the Lagrangian membrane forces calculated on the curvilinear mesh are distributed to the surrounding Eulerian fluid nodes on the fixed Cartesian mesh by a smoothed approximation of the delta function, where they enter the discretised lattice Boltzmann equation (2.1) as an external force term. The new fluid velocities are obtained after solving the LBM equation (2.1). The capsules are advected with the fluid velocity, where the velocity of each Lagrangian node on the membrane is interpolated from the surrounding Eulerian fluid node velocity using the same scheme as for the spreading of the forces. The distribution of the membrane forces $\boldsymbol{F}^m$ located at position $\boldsymbol{X}^m(\xi_1, \xi_2, t)$ to the adjacent fluid nodes is given by

$$\boldsymbol{f}(\boldsymbol{x}, t) = \int_{\Omega_S} \boldsymbol{F}^m(\xi_1, \xi_2, t)\delta(\boldsymbol{x} - \boldsymbol{X}^m(\xi_1, \xi_2, t))\,\mathrm{d}\Omega_S, \tag{2.9}$$

where δ is a three-dimensional approximation of the Dirac delta function, and $\boldsymbol{f}(\boldsymbol{x}, t)$ is the force density acting on the fluid at the Eulerian node $\boldsymbol{x}(x_1, x_2, x_3)$. Equation (2.9) is incorporated into (2.1) in a similar manner to an external body force (e.g. gravity) as follows

$$F_i(\boldsymbol{x}, t) = \left(1 - \frac{1}{2\tau}\right)\omega_i\left(\frac{\boldsymbol{c}_i - \boldsymbol{u}}{c_s^2} + \frac{\boldsymbol{c}_i \cdot \boldsymbol{u}}{c_s^4}\boldsymbol{c}_i\right)\cdot\boldsymbol{f}(\boldsymbol{x}, t). \tag{2.10}$$

The velocity of the membrane is obtained from the local Eulerian fluid velocity as

$$\frac{\partial \boldsymbol{X}^m}{\partial t} = \boldsymbol{u}(\boldsymbol{X}^m, t + \Delta t) = \int_{\Omega_D} \boldsymbol{u}(\boldsymbol{x}, t + \Delta t)\delta(\boldsymbol{x} - \boldsymbol{X}^m(\xi_1, \xi_2, t))\,\mathrm{d}x^3, \tag{2.11}$$

where Ω_D represents the whole fluid domain. Equation (2.11) enforces a no-slip boundary condition on the membrane, although in practice a volume drift is observed with time, and thus the need to use a penalty function on the volume (see (2.6)) or improved IBM schemes (Wu & Shu 2012; Casquero *et al.* 2020). Note the new fluid velocity $\boldsymbol{u}(\boldsymbol{x}, t + \Delta t)$ is obtained after solving the discretised lattice Boltzmann equation (2.1), which requires *a priori* knowledge of the membrane forces. The membrane forces $\boldsymbol{F}_k^m(t)$ are computed before solving (2.1), so to say, with respect to the old position of the membrane nodes $\boldsymbol{X}^m(t)$. Thus, the following notation $\boldsymbol{u}(t + \Delta t)$ is used in (2.11) instead of $\boldsymbol{u}(t)$. In discrete forms, (2.9) and (2.11) can be rewritten such that

$$\boldsymbol{f}(\boldsymbol{x}, t) = \sum_k \boldsymbol{F}_k^m(t)\delta(\boldsymbol{x} - \boldsymbol{X}_k^m(t))\Delta\Omega_{S,k} \tag{2.12}$$

$$\boldsymbol{u}(\boldsymbol{X}^m, t + \Delta t) = \sum_{\boldsymbol{x}} \boldsymbol{u}(\boldsymbol{x}, t + \Delta t)\delta(\boldsymbol{x} - \boldsymbol{X}^m(t))\Delta x^3, \tag{2.13}$$

where $\sum_k$ runs over the membrane nodes located within the interpolation range of a given fluid node $\boldsymbol{x}$, and $\sum_{\boldsymbol{x}}$ over a cuboidal region centred around a given membrane node $\boldsymbol{X}^m$.

The advection equation of a Lagrangian node on the capsule follows an explicit forward Euler scheme, such that

$$\boldsymbol{X}^m(\xi_1, \xi_2, t + \Delta t) = \boldsymbol{X}^m(\xi_1, \xi_2, t) + \boldsymbol{u}(\boldsymbol{X}^m, t + \Delta t)\Delta t. \tag{2.14}$$

Let us remark that, in principle, depending on the specific problem, one may need to tune the time step of the numerical integration of the Lagrangian dynamics independently from the lattice Boltzmann time step. For instance, for vanishing values of C, mesh instabilities can arise (owing to the formation of large wrinkles on the capsule surface). We have, therefore, decided to keep $C \geqslant 10^{-3}$ such that choosing the time step equal to the lattice Boltzmann Δt proved sufficient to prevent such instabilities.

The Dirac delta function in (2.9) and (2.11) is usually replaced with a smoother interpolation function (φ) of some shape such as $\delta(\boldsymbol{x}) = \varphi(x_1)\varphi(x_2)\varphi(x_3)$ to avoid jumps in velocities or in the applied forces occurring when the Lagrangian nodes do not coincide with the nodes of the Eulerian grid. Several distribution functions have been used in the IBM literature for a wide range of applications. For detailed reviews on the IBM and its accuracy, we refer the reader to Mittal & Iaccarino (2005) and Krüger *et al.* (2017) among other existing works on this topic. In what follows, we use a two-point linear interpolation function as discussed in Krüger (2012), which is given by

$$\varphi(\hat{x}) = \begin{cases} 1 - |\hat{x}| & \text{for } 0 \leqslant |\hat{x}| \leqslant 1 \\ 0 & \text{for } |\hat{x}| \geqslant 1 \end{cases}, \tag{2.15}$$

where $\hat{x}$ can denote x_1, x_2 or x_3.

2.4. *Simulations details, key parameters and observables*

We simulate shear flows, with constant shear rate $\dot{\gamma}$, in cubic boxes, seeded with N_p capsules of radius r. The computational domain has a side length $L = 128\Delta x = 16r$ and it is biperiodic along the flow and vorticity directions (x_1 and x_2 directions, respectively). It is bounded, in the x_3 direction, by two planar walls at which we impose a velocity boundary condition such to generate the driving shear flow as described in Hecht & Harting (2010).

The main control parameters of the problem are the volume fraction of capsules, $\phi = 4\pi r^3/3L^3$, the capillary number, Ca, and the membrane inextensibility, C (the particle scale Reynolds number being always so small, $Re = (\rho_0 \dot{\gamma} r^2)/\mu_0 < 10^{-1}$, that the dynamics can be considered effectively inertia-less). The capillary number, quantifying the relative intensity of viscous and elastic forces, is defined as

$$Ca = \dot{\gamma}\tau_{el}, \tag{2.16}$$

where $\tau_{el} = (\mu_0 r)/G_s$ is a time scale associated with the elasticity of the capsule. The value of C depends on the composition of the membrane. For example albumin–alginate capsules have a C of the order of unity (Carin *et al.* 2003), whereas for red blood cells $C \gg 1$.

Following Batchelor (1970), we evaluate the average particle stress tensor as

$$\Sigma^p_{ij} = \frac{1}{N}\sum_{\alpha=1}^{N} nS^{\alpha}_{ij} = -\frac{1}{V_D}\sum_{\alpha=1}^{N}\int_{\Omega_S}\frac{1}{2}\{F^{m,\alpha}_i X^{m,\alpha}_j + F^{m,\alpha}_j X^{m,\alpha}_i\}\,\mathrm{d}\Omega^{\alpha}_S, \tag{2.17}$$

where i and j are indices referring to Cartesian directions, $\sum_{\alpha=1}^{N_p}$ is a sum over the number of particles in the averaging volume V_D, n the number density and $\boldsymbol{S}$ the particle stresslet.

Here $\mathrm{d}\Omega_S^\alpha$ is the area element centred at $\boldsymbol{X}^m$, and $\boldsymbol{F}^m$ is the surface force density exerted by the membrane on the fluid. The rheology of the system is then assessed in terms of the suspension relative viscosity and normal stress differences. The relative viscosity of the suspension μ_r is defined as

$$\mu_r = \frac{\mu}{\mu_0} = 1 + \frac{\Sigma_{13}^p}{\mu_0 \dot{\gamma}}, \tag{2.18}$$

where μ is the effective viscosity of the system. The first and second normal stress differences can be deduced from the average particle stress tensor as

$$N_1 = \Sigma_{11}^p - \Sigma_{33}^p, \quad N_2 = \Sigma_{33}^p - \Sigma_{22}^p. \tag{2.19a,b}$$

The deformation of a capsule in the shear plane can be characterised in terms of the Taylor deformation parameter (Taylor 1934)

$$D = \frac{r_1 - r_3}{r_1 + r_3}, \tag{2.20}$$

where r_1 and r_3 are the major and minor principal semi-axes (in the shear plane) of an ellipsoid having the same tensor of inertia as the deformed capsule, and the inclination angle θ, which is the angle the major axis forms with the positive direction of the x_1-coordinate (see figure 1). The ellipsoid principal semi-axes are defined as (Ramanujan & Pozrikidis 1998; Li & Sarkar 2008; Frijters, Günther & Harting 2012; Farutin *et al.* 2014):

$$r_1 = \sqrt{\frac{5}{2\rho_0 V}(I_2 + I_3 - I_1)}, \quad r_2 = \sqrt{\frac{5}{2\rho_0 V}(I_1 + I_3 - I_2)}, \quad r_3 = \sqrt{\frac{5}{2\rho_0 V}(I_1 + I_2 - I_3)}, \tag{2.21a–c}$$

where I_1, I_2 and I_3 are the eigenvalues of the tensor of inertia.

The rheology and microstructure of suspensions of strain-hardening capsules up to a volume fraction of 0.5 are studied for capillary numbers ranging from $Ca = 0.1$ to 1. The number of particles is varied from 1 to 500, corresponding to $\phi \approx 0.001$ and $\phi \approx 0.5$, respectively. Each particle is discretised with 1280 triangles and 642 nodes, and initialised as a sphere with a radius $r = 8\Delta x$. When the distance between two neighbouring particles is below $1\Delta x$, a repulsive force acts on the surface of the two particles with an interaction strength chosen as $\bar{\epsilon} \approx 10^2 G_s r$. The simulations are initialised with the capsules distributed randomly in the domain with an initial radius $r_0 < r$. The radius of each capsule is then increased in time with a fixed growth rate until reaching the desired size. The relative error on the capsule's volume defined as $\epsilon_V = |V - V_0|/V_0$ is below 0.03 % in all simulations. For suspensions, the measured quantities are obtained from an average over the number of particles and over time. In terms of strain units ($\dot{\gamma}t$), our simulations reach convergence after the first 5–7$\dot{\gamma}t$. The time average is performed after the initial transient state defined here as the first $10\dot{\gamma}t$. Time histories of the mean deformation and relative viscosity in the dilute and semi-dilute limits, together with the effect of mesh discretisation and finite size effects, are shown in appendix A. Details on the performance of our code can be found in Aouane *et al.* (2018).

3. Results

3.1. *Behaviour of a single capsule in a shear flow*

In order to validate our approach, we first limit our simulations to the case of single initially spherical Skalak capsules. Our simulation domain is bounded by two parallel walls and

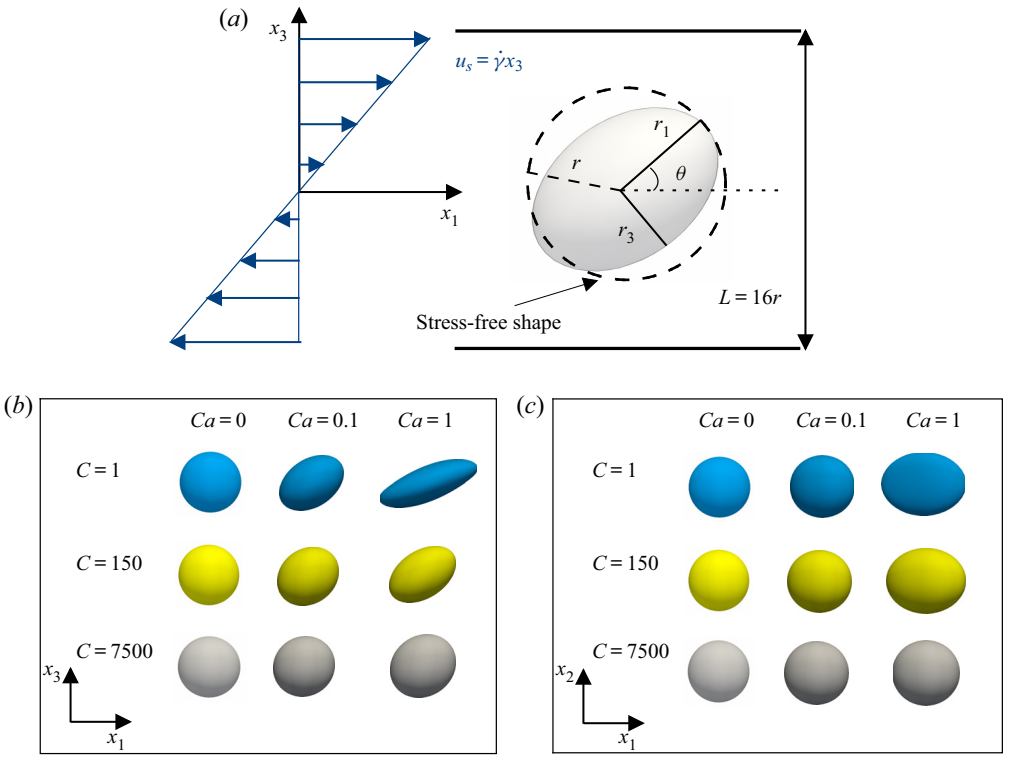

Figure 1. (*a*) Schematic of a single capsule in a shear flow showing the initial (dashed lines) and the typical ellipsoidal steady-state shapes; r is the radius of the unstressed sphere, r_1 and r_3 are the major and minor semi-axes in the shear plane (r_2 is that in the vorticity direction, not shown) and θ is the inclination angle. (*b*,*c*) Numerically computed steady-state shapes for different values of C and Ca namely in the x_3x_1-plane (defined between the shear gradient and flow directions) and x_2x_1-plane (defined between the vorticity and the flow directions).

the confinement is set to $\chi = 2r/L = 0.125$, so that the effect of the boundaries can be neglected. A schematic representation of the simulation setup, together with examples of steady state shapes for different Ca and C, are depicted in figure 1. The steady Taylor deformation parameter, the inclination angle, the normal stress difference and the intrinsic viscosity, defined as

$$[\mu] = \lim_{\phi \to 0} \frac{\mu_r - 1}{\phi}, \tag{3.1}$$

as functions of Ca (for different values of C) are plotted in figure 2. We compare with numerical results obtained using the boundary element method (Lac *et al.* 2004) and the front-tracking method (Bagchi & Kalluri 2010), showing good agreement.

We next move to explore systematically the parameter space spanned by (Ca, C), with $Ca \in [0.1; 1]$ and $C \in [1; 7500]$. The corresponding data on steady-state elongation, inclination angle, intrinsic viscosity and first normal stress difference are reported in figure 3. We see, from the symbols in figure 3(*c*), at fixed C, that $[\mu]$ decreases with Ca, denoting a shear-thinning character. The latter, in turn, appears to be directly correlated to an increase of the elongation of the capsule (figure 3*a*) and a decrease of its orientation with respect to the flow direction (figure 3*b*), similarly to what has been reported for drops, vesicles and strain-softening capsules. Moreover, a clear effect of C on the various

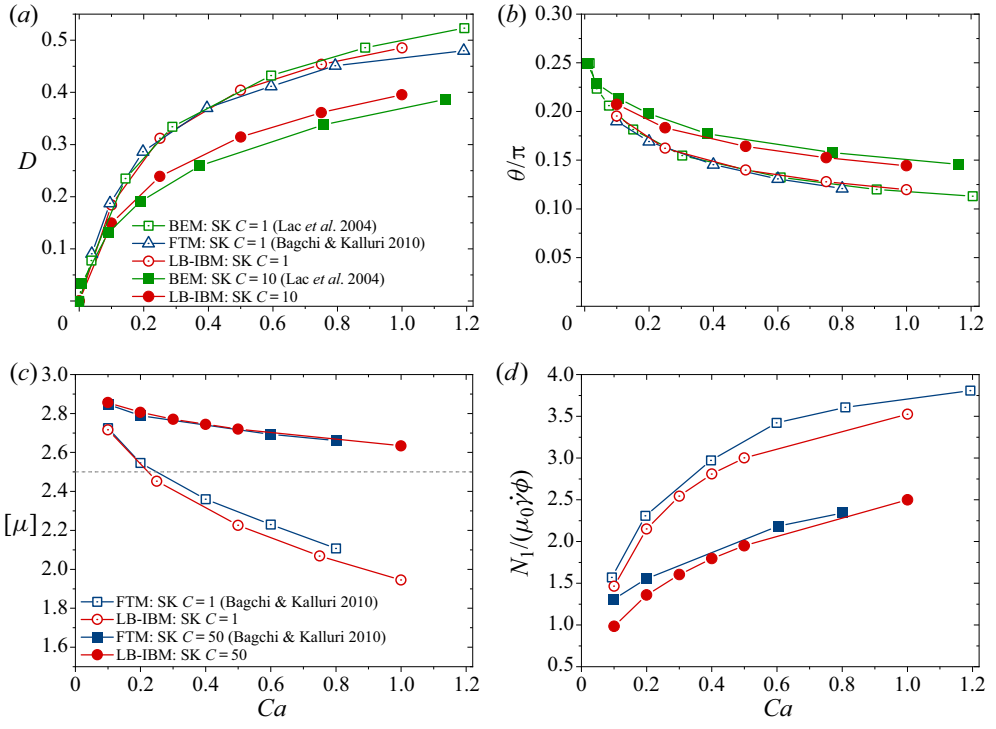

Figure 2. Steady Taylor deformation parameter (*a*), inclination angle (*b*), intrinsic viscosity (*c*), and first normal stress difference (*d*) of a single capsule under a shear flow. The open and full symbols in (*a*,*b*) are for $C = 1$ and $C = 10$, respectively, and for $C = 1$ and $C = 50$ in (*c*,*d*). BEM denotes the boundary element simulations of Lac *et al.* (2004), and FTM the front-tracking method of Bagchi & Kalluri (2010). LBM-IBM are the numerical results obtained using our lattice Boltzmann code. The dashed line in (*c*) indicates the value of the intrinsic viscosity of a dilute suspension of rigid spheres. The legends for (*b*,*d*) are indicated in (*a*,*c*), respectively.

observables can be detected: as C grows, their dependence on Ca gets weaker. In particular, the steady Taylor parameter D suggests that the particle is less and less deformed, i.e. it approaches the limit of a rigid sphere. Correspondingly, $[\mu]$ varies less and less with Ca and eventually the shear-thinning is suppressed. For sufficiently large C, then, a very dilute suspension of strain-hardening capsules tends to behave rheologically as a suspension of rigid spheres (note also that N_1 tends to zero, figure 3*d*), albeit with an intrinsic viscosity surprisingly slightly larger than the Einstein coefficient $[\mu] = 5/2$ (for $C \gg 1$, $[\mu]$ seems to approach the limiting value ≈ 2.84; see also Bagchi & Kalluri (2010) for comparison).

3.2. *Suspensions: structure*

We investigate the multiparticle case and the dependence of particle shape and suspension rheological properties on the parameters describing the system, namely Ca, C and ϕ. Examples of steady-state configurations of the suspension are shown in figure 4, for fixed $Ca = 1$, $\phi = 0.5$ and for four different values of $C = 0.1$, 10, 150 and 7500.

In this subsection we focus on particle morphologies, characterised in terms of the Taylor deformation parameter and the semi-axes of the equivalent ellipsoid, whereas in the next we study the rheological properties of the suspensions, highlighting their relations with the structure. Analogously to the single-particle case, the mean Taylor parameter $\langle D \rangle$

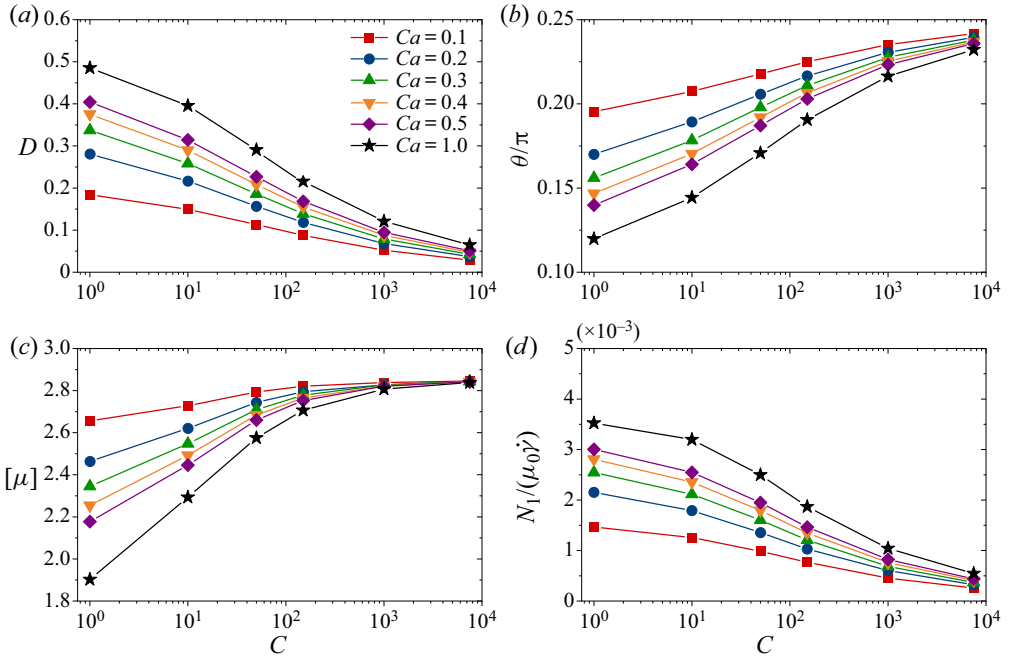

Figure 3. Effect of the membrane area incompressibility on the steady-state Taylor deformation parameter (*a*), inclination angle (*b*), intrinsic viscosity (*c*) and first normal stress difference (*d*) of a single Skalak capsule under a shear flow for different capillary numbers. The legend is given in (*a*).

of the suspension decreases with increasing C (figure 5*a*), with a steepest descent for $1 < C < 10^3$, which confirms that capsules become less deformable and tend to resemble rigid particles. We recall, though, that such a parameter contains information only on two of the three semi-axes of the equivalent ellipsoid. To get a deeper insight, then, we present all three of them separately in figure 5(*b–d*). Interestingly, a non-monotonic behaviour is found for $\langle r_1 \rangle$ and $\langle r_2 \rangle$ (the semi-axes in the flow and vorticity directions, respectively) for $0.1 < C < 10$. In particular, for decreasing $C < 10$, $\langle r_2 \rangle$, whose direction is orthogonal to the elongational one, grows. Moreover, $\langle r_2 \rangle$ always remains larger than $\langle r_3 \rangle$, indicating that particles, on average, are not spheroids (eventually, for very large C particles approach the undeformable limit and the quasi-spherical shape, $\langle r_i \rangle \to r$ for $i = 1, 2, 3$, is recovered). In this sense, capsules display a lower level of symmetry than droplets, which is to be attributed to the nonlinear elastic characteristics of the membrane. The behaviour, in fact, persists across the various volume fractions explored, even for the lowest ϕ (corresponding to the single-particle case), suggesting that the effect originates from the properties of the single-particle stress tensor. The spread of the mean principal semi-axes, mostly of $\langle r_1 \rangle$, is such that the product $\prod_{i=1}^{3} \langle r_i \rangle$ varies with the volume fraction. Such dependence is related to the variances of the distributions of the principal semi-axes (given that the mean volume of capsules, $\langle \prod_{i=1}^{3} r_i \rangle$ is conserved) and reflects, therefore, the spread in sizes, which decreases as C increases, because the capsules become more and more rigid (in other words, the distribution tends to become sharply peaked around $r_1 \sim r_2 \sim r_3 \sim r$).

Next, we consider how the particle deformation depends on the applied load, for given material properties. It is tempting, first, to investigate how the peculiar behaviour for small/moderate C shows up across different shear values. In figure 6(*a–c*) we report the

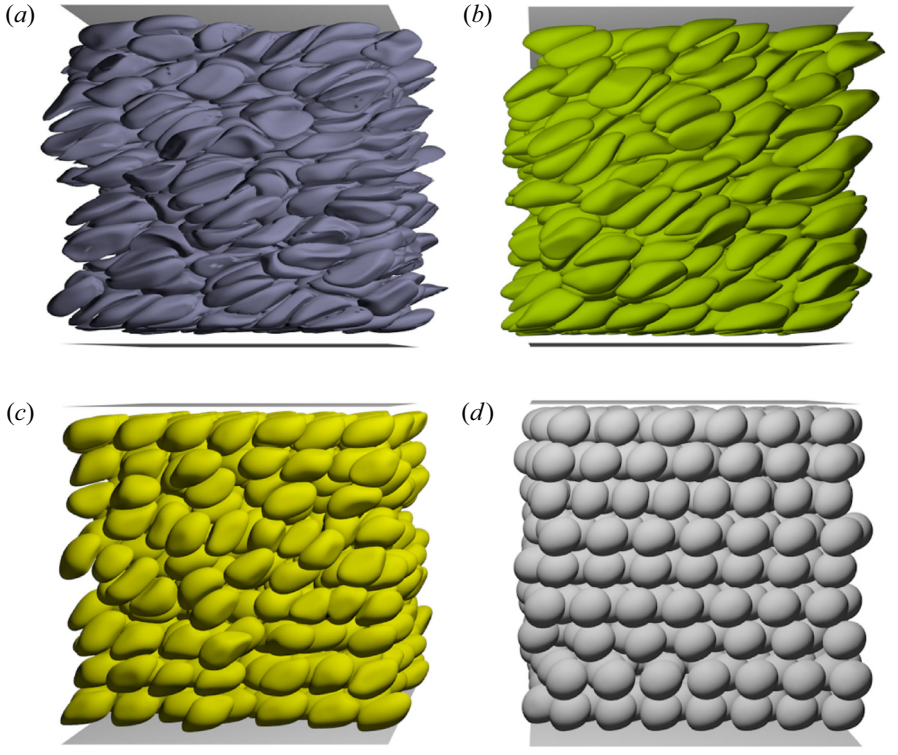

Figure 4. Steady-state configurations for $\phi = 0.5$, $Ca = 1$ and (*a*) $C = 0.1$, (*b*) $C = 10$, (*c*) $C = 1.5 \times 10^2$ and (*d*) $C = 7.5 \times 10^3$.

variation of r_i for single capsules with $C = 0.1$, 1 and 10, respectively, as a function of Ca. As Ca increases, the capsules become, obviously, more elongated in the extensional flow direction (r_1 grows), but the two minor semi-axes display opposite trends, depending on the value of C: whereas r_3, as expected, decreases (for all C), r_2 (that aligned with the vorticity direction) grows for $C < 1$. For the smallest C considered, $C = 0.1$, we need, therefore, to find an equivalent breadth, $r_\perp^{(eq)}$ quantifying the degree of shrinkage or expansion of the capsule in the equatorial plane. We define this $r_\perp^{(eq)}$ as the ratio of the length of the membrane cross-section (an ellipse) over 2π (such that it would be precisely the minor axis, if the capsule were a prolate spheroid), i.e. $r_\perp^{(eq)} = 4r_2\mathcal{E}(\epsilon(r_2, r_3))/2\pi$, where $\mathcal{E}(x)$ is the complete elliptic integral of the second kind (Abramowitz & Stegun 2012) and $\epsilon(r_2, r_3) = \sqrt{1 - (r_3/r_2)^2}$ is the eccentricity of the ellipse. In figure 6(*d*), we plot the transversal deformation, represented by $r_\perp^{(eq)}$ versus the elongation, $r_{||} \equiv r_1$, both normalised by the rest radius r, for the capsule with $C = 0.1$. It can be seen that, although $r_\perp^{(eq)}/r$ never exceeds 1, i.e. overall the membrane cross-section shrinks with respect to the equilibrium shape, there is a range of Ca for which it expands as the capsule is elongated. This is an intriguing behaviour, in fact the opposite of the slope of the curve in figure 6(*d*), $\tilde{\nu}_s = -\mathrm{d}r_\perp^{(eq)}/\mathrm{d}r_{||}$, can be interpreted as a *local* Poisson's ratio, which is negative for $1.3r \lesssim r_{||} \lesssim 1.7r$. This observation hints at a sort of local (in shear) 'auxeticity' (Evans *et al.* 1991) of membranes obeying a Skalak-type constitutive law with low values of the membrane inextensibility parameter.

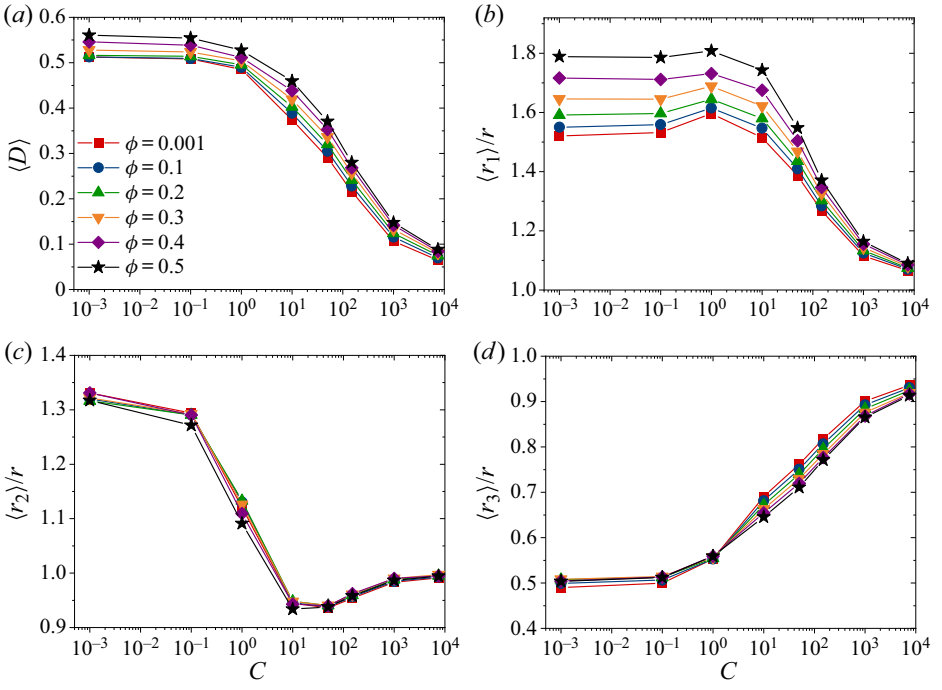

Figure 5. (*a*) Steady-state Taylor deformation parameter. (*b*)–(*d*) Steady-state mean semi-axes of the capsules normalised by the reference radius as function of C for different values of ϕ. The legend is indicated in (*a*). Here $Ca = 1$.

In figure 7(*a*) we show the average Taylor deformation parameter as function of Ca, for various ϕ. Two sets of data corresponding to $C = 50$ (closed symbols) and $C = 150$ (open symbols) are reported. The deformation grows as $\langle D\rangle \sim Ca$ for small capillary numbers, as expected, and then sublinearly as the Ca increases (eventually we observe a logarithmic dependence $\langle D\rangle \sim \log(Ca)$, in agreement with previous numerical Dodson III & Dimitrakopoulos (2010) and experimental Hardeman *et al.* (1994) findings), reflecting the strain-hardening character of the capsules. It can be asked whether one may find a functional form that allows to recast the variability among curves into a single curve-shape parameter, $Ca^*(\phi, C)$, that is

$$\langle D\rangle \equiv \mathcal{D}(Ca, \phi, C) = Ag\left(\frac{Ca}{Ca^*(\phi, C)}\right), \tag{3.2}$$

where A is a constant prefactor and the function $g(x)$ has to be chosen such that it reproduces and connects both behaviours at small and large Ca, that is $g(x) \sim x$ as $x \to 0$ and $g(x) \sim \log(x)$ for $x \gg 1$. This is indeed possible and we show it in figure 7(*a*). There, the fits, indicated by the dashed lines, are obtained from (3.2), choosing for the function g the expression $g(x) = \log(1 + x)$, with the same $A = 0.1$ and, from bottom to top, $Ca^* = 0.13$, $Ca^* = 0.07$ and $Ca^* = 0.037$, respectively. For a fixed capillary number, $\langle D\rangle$ increases linearly with the volume fraction ϕ, similarly to suspensions of drops and neo-Hookean capsules (Loewenberg & Hinch 1996; Matsunaga *et al.* 2016). Conversely, the larger is the membrane inextensibility C, the less deformed are the capsules.

Given the self-similar form of (3.2), we would like to find a universal curve for $\langle D\rangle$, through a proper definition of an effective capillary number Ca_{eff}. The enhancement of

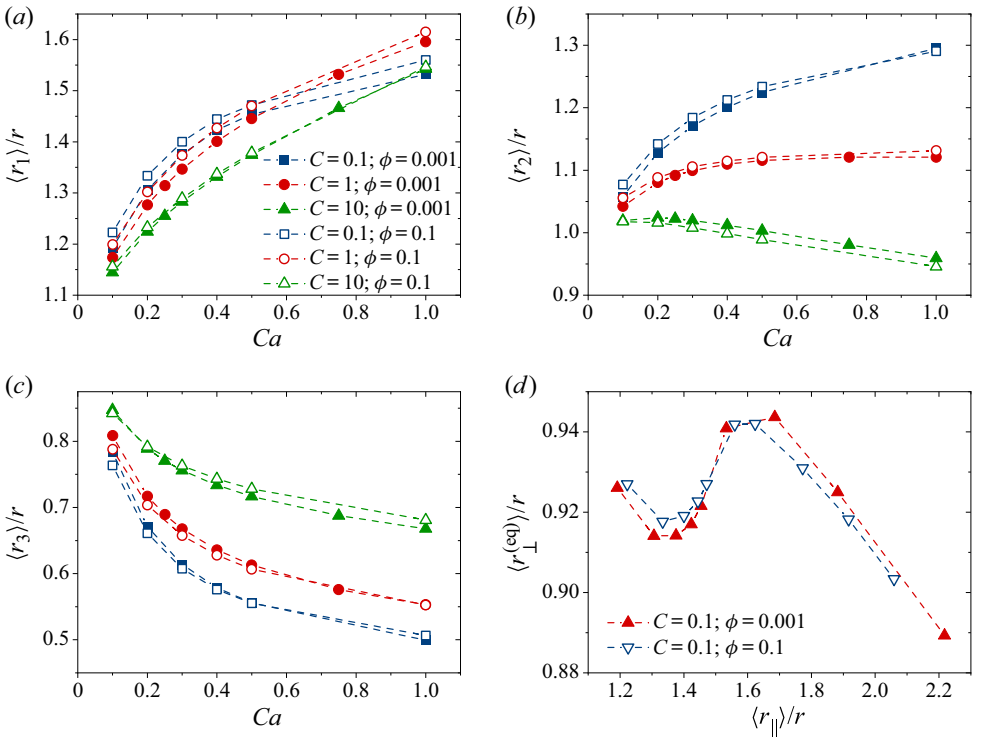

Figure 6. (*a*)–(*c*) Steady-state semi-axes (normalised by the reference radius of the initially spherical stress-free capsule) as a function of Ca for capsules with $C = 0.1$, 1 and 10, respectively (the legend is indicated in (*a*)). (*d*) Transversal deformation versus elongation (normalised by the reference radius) for capsules with $C = 0.1$, and $Ca \in [0.1; 7.5]$. Open symbols refer to $\phi = 0.1$ (semi-dilute suspension), whereas full symbols to $\phi = 0.001$ (dilute suspension).

deformation with ϕ can be interpreted as an effect of larger viscous stresses around the particle, owing to the fact that the effective viscosity of the suspension increases with the volume fraction (this aspect will be discussed in more detail in the next subsection). This suggests that we should replace, in Ca_{eff}, the 'bare' dynamic viscosity with the effective one, $\mu_0 \to \mu_{eff} = \mu_0(1 + [\mu]\phi)$. Here we assume, for simplicity, linearity in ϕ and a constant (with Ca and C) intrinsic viscosity, equal to its large C limit, $[\mu] \approx 2.8$ (see § 3.1).

Furthermore, we note that for a non-zero membrane inextensibility, it is more appropriate to base the capillary number on the Young's modulus instead of the shear modulus (Barthès-Biesel & Rallison 1981). We propose to replace G_s with $E_s = ((2 + 4C)/(1 + C))G_s$. However, this might not be sufficient. In fact, the imposed constraint of volume conservation, for a spherical equilibrium shape, effectively entails an extra tension on the surface, because the capsules tend to become essentially undeformable as the area dilatation modulus is increased. This can be accounted for by the substitution

$$E_s \to E_s^{(eff)} = \frac{(2 + 4C)}{(1 + C)} G_s^{(eff)} = \frac{(2 + 4C)}{(1 + C)}(1 + \beta C)G_s \tag{3.3}$$

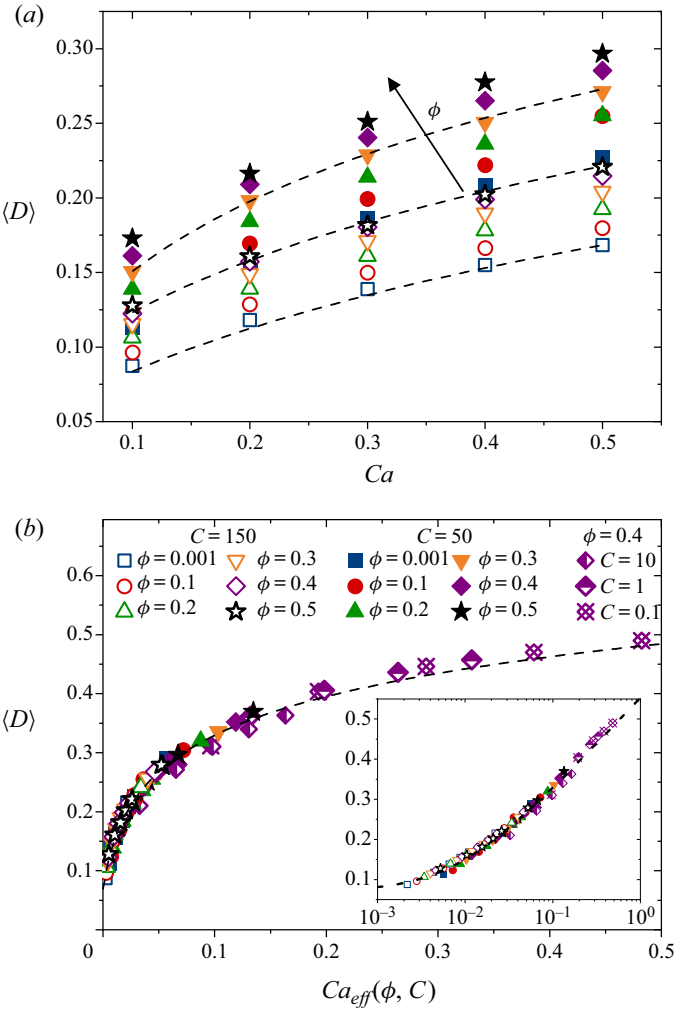

Figure 7. (*a*) Mean Taylor deformation parameter for a suspension of strain-hardening capsules as a function of Ca, for two values of membrane inextensibility, $C = 50$ (filled symbols) and $C = 150$ (open symbols). The dashed lines are fits of the numerical data using (3.2) with $A = 0.1$ and (from bottom to top) $Ca^* = 0.13$, $Ca^* = 0.07$ and $Ca^* = 0.037$, respectively. The arrow indicates a growing volume fraction ϕ. (*b*) Mean Taylor deformation parameter as a function of the effective capillary number (3.4). The dashed line corresponds to the fitting function (3.2) ($A_{eff} = 0.1$ and $Ca^*_{eff} = 4 \times 10^{-3}$). Inset: Lin-Log plot of $\langle D \rangle$ vs Ca_{eff}, highlighting the logarithmic behaviour for $Ca_{eff} > Ca^*_{eff}$. The legend is indicated in (*b*).

(β being a free parameter, which we set hereafter to $\alpha = 0.07$) in the effective capillary number, which then finally reads

$$Ca_{eff}(\phi, C) = \frac{\mu_{eff}\dot{\gamma} r}{E_s^{(eff)}} = \frac{(1 + [\mu]\phi)(1 + C)}{(2 + 4C)(1 + \beta C)} \left(\frac{\mu_0 \dot{\gamma} r}{G_s} \right) \equiv \frac{(1 + [\mu]\phi)(1 + C)}{(2 + 4C)(1 + \beta C)} Ca. \quad (3.4)$$

When plotted as a function of Ca_{eff}, the values of $\langle D \rangle$ for different ϕ and C collapse onto a single master curve, as shown in figure 7(*b*). Such a curve can also be fitted using (3.2), with $A = 0.1$ and $Ca^*_{eff} = 4 \times 10^{-3}$. Note that the existence of a single Ca^*_{eff} capable to

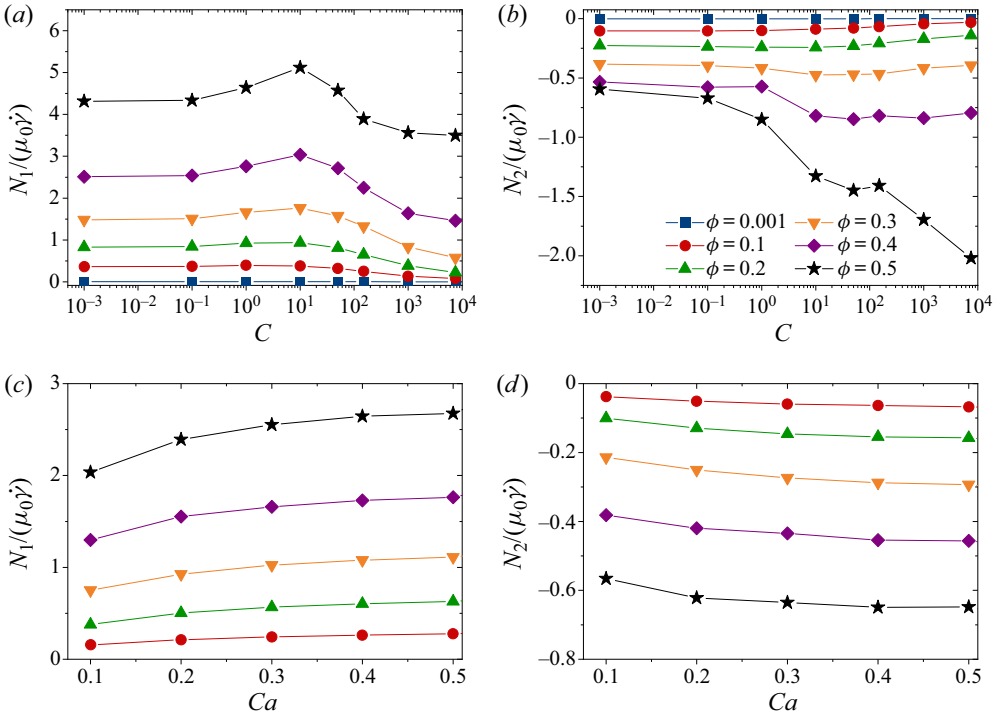

Figure 8. Normal stress differences (normalised by the dynamics viscosity of the fluid times the applied shear) as a function of C for $Ca = 1$ (*a*,*b*) and as function of Ca for $C = 1$ (*c*,*d*). The legend is shown in (*a*).

fit all data sets upon the rescaling (3.4) is equivalent to saying that the dependence of the curve-shape parameter Ca^* on Ca and C is such that $Ca^* \propto G_s^{(eff)}(C)/\mu_{eff}(\phi)$.

3.3. *Suspensions: rheology*

We now consider the rheological response of the system by looking at the suspension relative viscosity and normal stress differences. In figure 8, we plot N_1 and N_2 (normalised by $\mu_0\dot{\gamma}$), for various volume fractions, for $Ca = 1$ as a function of the membrane inextensibility (figure 8*a*,*b*) and for $C = 1$ as a function of the capillary number (figure 8*c*,*d*). We see that both (though N_2 only weakly) show a non-monotonic dependence on C, a behaviour that is enhanced as ϕ is increased. In particular, N_1 initially grows with C, reaches a peak at $C \approx 10$, and then starts to decrease. For emulsions and strain-softening capsules, the magnitude of N_1 is significantly larger than the magnitude of N_2, whereas the opposite is true for suspensions of rigid particles. Here N_1 and N_2 are known to be correlated to hydrodynamic interaction, and particle–particle collisions, respectively (Guazzelli & Pouliquen 2018). We find that for strain-hardening capsules N_1 is positive and grows monotonically with Ca, whereas N_2 has a negative sign and decreases with Ca (in qualitative agreement with what found for suspensions of strain-softening capsules Matsunaga *et al.* 2016). The magnitude of N_1 is always larger than N_2, but the ratio $|N_1|/|N_2|$ diminishes with the increase of C. It seems, therefore, in principle possible, by tuning their deformability through C, to make collections of such soft particles behave rheologically more as solid suspensions or as emulsions and suspensions of strain-softening capsules.

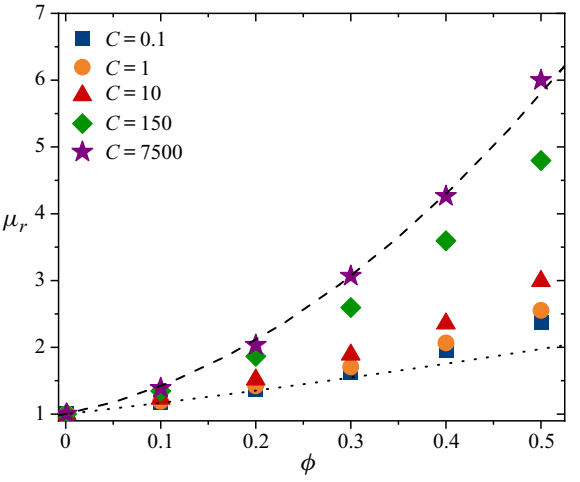

Figure 9. Relative viscosity as function of the volume fraction for several values of C and $Ca = 0.5$. The curves correspond to (3.5) with $[\mu] = 1.63$, $K = 0.64$ (dotted line) and $[\mu] = 2.84$, $K = 13.5$ (dashed line), respectively.

To delve deeper into this aspect, we study how the dependence of the relative viscosity of the suspension on the capsule volume fraction changes with C. We report in figure 9 the behaviour of μ_r versus ϕ for $Ca = 0.5$ and various C. The relative viscosity of a suspension can be expressed as a polynomial function of the volume fraction as

$$\mu_r = 1 + [\mu]\phi + K\phi^2 + O(\phi^3), \tag{3.5}$$

where $[\mu]$ is the intrinsic viscosity and the second-order term accounts for pair hydrodynamic interactions and allows to expand the validity of (3.5) to semi-dilute cases (Batchelor & Green 1972). All data sets in figure 9 can be reasonably well fitted by a quadratic relation of the type (3.5). As C increases, the data tend to approach a limiting curve with $[\mu] = 2.84$ and $K = 13.5$ (dashed line), whereas for low C they tend to agree well with the curve (dotted line) for strain-softening particles reported in Matsunaga *et al.* (2016).

In figure 10(*a*) we extend the study of the relative viscosity to a range of capillary numbers, $Ca \in [0.1, 0.5]$, in order to analyse the response of the system to changes in the applied shear. The shear-thinning character of the suspension of capsules can be appreciated: for a given volume fraction, in fact, μ_r tends to decrease with Ca (the larger ϕ the more evident is the shear-thinning), but the spread is reduced for larger C, i.e. the shear-thinning tends to be suppressed, confirming that also for semi-dilute and moderately concentrated regimes, the rheology of suspensions of strain-hardening capsules resemble that of solid suspensions. In order to find a universal behaviour of the relative viscosity across the various shear rates, recently Rosti, Brandt & Mitra (2018) introduced, for suspensions of deformable viscoelastic spheres (and Takeishi *et al.* (2019) extended to the case of red blood cells), the notion of a reduced *effective* volume fraction, calculated using for the particle volume (when they are in the deformed state), that of a sphere with a radius equal to the smallest particle semi-axis r_3, i.e. $\Phi_{eff} = \frac{4}{3}\pi r_3^3$. The rationale behind this approach is that the dynamically 'active' direction is the velocity gradient (wall-normal direction) and, because the deformed particles do not tumble and tend to align with the flow direction, then the relevant length is the minor axis. For r_3, the average value as measured in the simulations was taken. Here, we propose to relate r_3 to the radius at rest

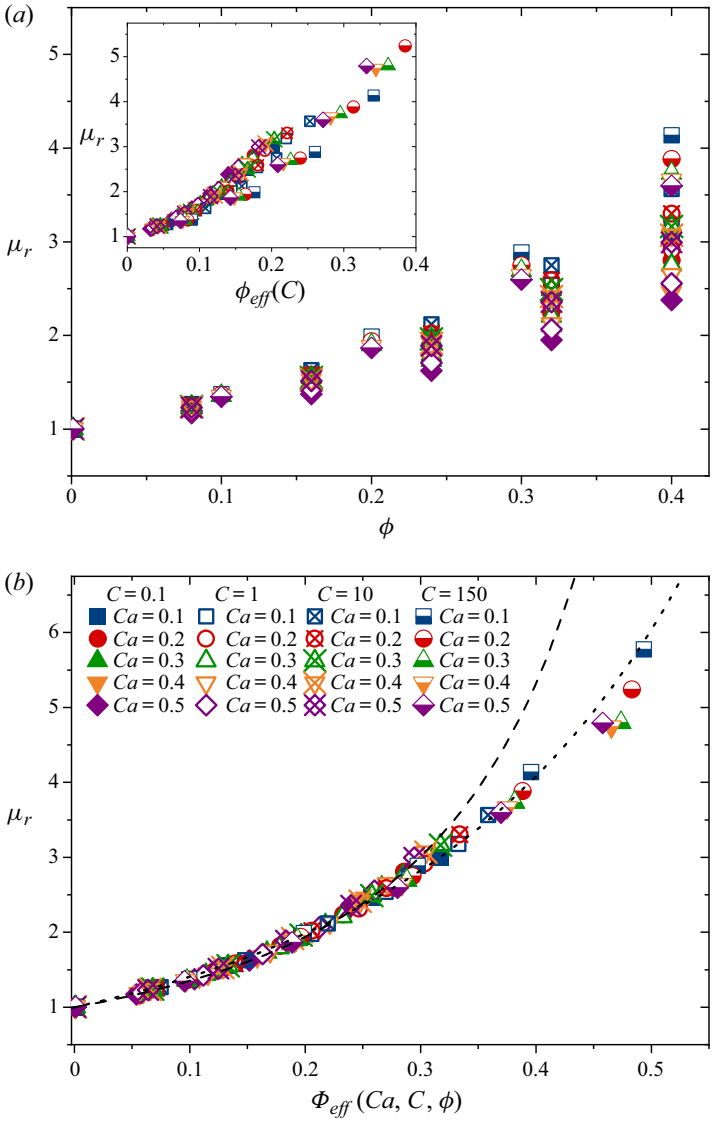

Figure 10. (*a*) Relative viscosity as a function of the volume fraction for different Ca and C. The inset shows μ_r plotted as function of the effective volume fraction as defined in (3.8). The legend of (*a*) is shown in (*b*). (*b*) Relative viscosity as a function of the effective volume fraction (see (3.9)). The dashed line corresponds to a fit of the numerical data using (3.10), with $B = 1.4$ and $\Phi_m = 0.7$. Same for the dotted line but with $B = 1.7$ and $\Phi_m = 1.2$

r through the Taylor deformation parameter D. To this aim, let us assume the particles to be prolate ellipsoids with $r_1 > r_2 = r_3$ (this is an approximation that allows to close the problem, although we know that the specific relation among the three axes depends on the value of membrane inextensibility C). Here r_1 and r_3 enter into the expression of D (2.20), that can be inverted as

$$r_1 = \frac{1+D}{1-D} r_3. \tag{3.6}$$

Owing to volume conservation we have $r^3 = r_1 r_3^2$ and therefore $r^3 = ((1+D)/(1-D))r_3^3$, which implies

$$r_3 = \left(\frac{1-D}{1+D}\right)^{1/3} r. \tag{3.7}$$

If we now define, as in Rosti *et al.* (2018), the effective volume fraction as $\Phi_{eff} \equiv \frac{4}{3}\pi\langle r_3\rangle^3 n$ and assume (3.7) to be valid also for average quantities in the suspension, we obtain

$$\Phi_{eff} = \frac{1-\langle D\rangle}{1+\langle D\rangle}\phi. \tag{3.8}$$

As we learned from the previous section, $\langle D\rangle$, in turn, depends on ϕ, on the capillary number and on C. If we plug (3.2) inside (3.8), with the rescaled effective capillary number, (3.4), and we plot μ_r as a function of the obtained Φ_{eff}, we observe a reasonable overlap of the data, although with some deviations, especially for the largest values of C (see inset of figure 10*a*). We ascribe this partial failure to the fact that our strain-hardening capsules are not precisely aligned with the flow direction (see figure 2*b*). Consequently, the relevant, flow-orthogonal, length is not exactly r_3, but the vertical semi-axis of the ellipse, resulting as the section of the particle ellipsoid on a plane perpendicular to the flow direction (and crossing its centre). It is easy to show, by geometrical arguments, that such length is $\ell = r_3\sqrt{((1+b^2)/(1+(r_3/r_1)^2 b^2))}$, where $b = \tan(\theta)$, and θ is the inclination angle. If we define the effective volume fraction in terms of this length (and recalling that $r_3/r_1 = (1-D)/(1+D)$), equation (3.8) becomes

$$\Phi_{eff} = \frac{1-\langle D\rangle}{1+\langle D\rangle}\left(\frac{1+b^2}{1+\left(\dfrac{1-\langle D\rangle}{1+\langle D\rangle}\right)^2 b^2}\right)^{3/2}\phi. \tag{3.9}$$

The parameter b itself depends, through θ, on Ca and C. However, for simplicity, we consider it here as a fit constant, taking for θ values restricted to the range in figure 2(*b*). In particular, for $\theta = \pi/5$ ($b \approx 0.726$), we get a nice collapse of all data sets onto a single master curve which can be well fitted, among others, with an Eilers function (Eilers 1941)

$$\mu_r(\Phi_{eff}) = \left[1 + \frac{B\Phi_{eff}}{1-\dfrac{\Phi_{eff}}{\Phi_m}}\right]^2, \tag{3.10}$$

with parameters $B = 1.4$ and $\Phi_m = 0.7$ (figure 10*b*). Choosing $B = 1.7$ and $\Phi_m = 1.2$ also the branch at large Φ_{eff} can be fitted, but these are somehow not sound values. We argue, instead, that the deviations from the Eilers fit (which occur for the set of data corresponding to the largest $C = 150$ and $\phi = 0.4, 0.5$) are due to the fact that under these conditions important hydrodynamic correlations emerge which cannot be simply adhered to a reduced volume effect. Let us stress that the relation (3.8), as much as in the approach of Rosti *et al.* (2018), needs an empirical input (the function $g(x)$ in (3.2)). However, for small effective capillary number, it is possible to approximate g with its linear part, thus providing a closed and explicit expression for $\Phi_{eff}(Ca, C, \phi)$ and, consequently, an explicit dependence of the relative viscosity μ_r on Ca, C and ϕ.

4. Conclusions

The rheology of a suspension of strain-hardening capsules is investigated numerically from the dilute to the concentrated regimes in a simple shear flow. We have addressed the role of the membrane inextensibility, C, on the capsule shape and on the suspension rheology, at varying the volume fraction, ϕ, and the capillary number, Ca (based on the applied shear). Our results indicate that increasing the membrane inextensibility makes the capsules less deformable, and as a consequence the shear-thinning character of the suspension is hindered. We show that, upon a proper definition of an effective C- and ϕ-dependent capillary number, the mean Taylor deformation parameters relative to various data sets collapse onto a single master curve. However, it proved necessary to go beyond the deformation parameter, in order to get a deeper insight on the complex impact the membrane inextensibility has on the full three-dimensional capsule shape. The three principal semi-axes displayed, in fact, a non-monotonic dependence on C, and for small C ($C = 0.1$) and a certain range of Ca, an auxetic behaviour of the capsules was observed. The characteristic shape behaviour was reflected in a non-monotonic dependence of the first normal stress difference with the membrane inextensibility. Finally, the rheological response of the suspension has been analysed also in terms of its relative viscosity. The latter showed a universal behaviour across the various concentrations, shear rates and membrane inextensibilities explored, once an effective volume fraction, taking into account the capsules elongation and orientation, was introduced.

Acknowledgements. We are grateful to M. Léonetti for fruitful discussions and to the referees for their comments and suggestions. The authors gratefully acknowledge the computing time granted by the John von Neumann Institute for Computing (NIC) and provided on the supercomputer JURECA at Jülich Supercomputing Centre (JSC), by the High Performance Computing Center Stuttgart (HLRS) on the Hazel Hen supercomputer and by the Regional Computing Centre Erlangen (RRZE).

Funding. The authors acknowledge financial support by the Deutsche Forschungsgemeinschaft (DFG) within the Cluster of Excellence 'Engineering of Advanced Materials' (project EXC 315) (Bridge Funding), and within the research unit FOR2688 'Instabilities, Bifurcations and Migration in Pulsatile Flows' (grant number HA4382/8-1). This work was also supported by the Competence Network for Scientific High-Performance Computing in Bavaria (KONWIHR III, project 'Dynamics of Complex Fluids') and the European Cooperation in Science and Technology (COST) Action MP1305: 'Flowing Matter'.

Declaration of interests. The authors report no conflict of interest.

Author ORCIDs.
Othmane Aouane https://orcid.org/0000-0002-5267-1629;
Andrea Scagliarini https://orcid.org/0000-0002-3893-746X;
Jens Harting https://orcid.org/0000-0002-9200-6623.

Appendix A

A.1. *Particle discretisation and mesh quality*

Our membrane is discretised using triangular elements. The spherical capsule results from refining an icosahedron recursively N_r times. The total number of faces denoted N_f is defined from the total number of vertices N_v and the number of recursive refinement such as $N_f = 2N_v - 4$ and $N_v = 2 + 10 \cdot 4^{N_r}$. In this work, we used $N_r = 3$ leading to $N_v = 642$ and $N_f = 1280$. To study the effect of the mesh discretisation on the shape and rheology, we varied N_r from 2 to 4, which corresponds namely to $N_f = 320$ and $N_f = 5120$. We set C to unity to test situations with large deformations.

N_f	320	1280	5120
r_1/r	1.429 ± 0.027	1.445 ± 0.028	1.442 ± 0.027
r_2/r	1.095 ± 0.012	1.117 ± 0.0145	1.116 ± 0.0138
r_3/r	0.61 ± 0.023	0.612 ± 0.024	0.619 ± 0.024
D	0.401 ± 0.024	0.404 ± 0.025	0.398 ± 0.024
θ/π	0.138 ± 0.007	0.139 ± 0.007	0.139 ± 0.007
$[\mu]$	2.109 ± 0.124	2.226 ± 0.129	2.25 ± 0.133

Table 1. Steady-state shape and rheology quantities (time averaged) for $Ca = 0.5$ and $C = 1$.

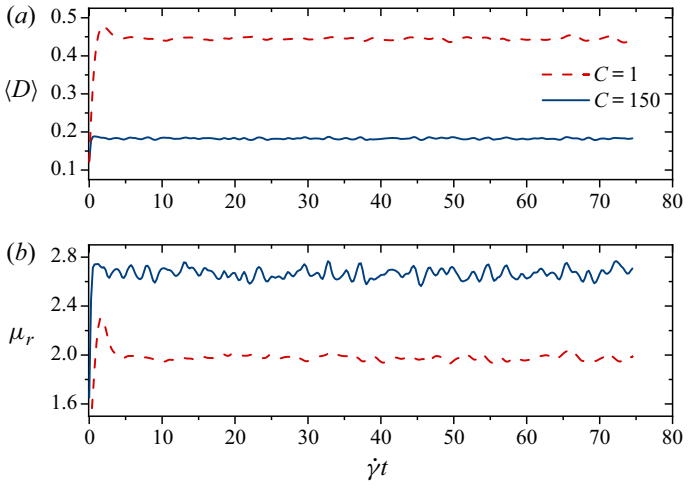

Figure 11. (*a*) History of the mean deformation and (*b*) the relative viscosity of the capsules for a semi-dilute suspension ($\phi = 0.3$) and two different membrane inextensibilities ($C = 1, 150$).

We report in table 1 some of the relevant quantities measured for different number of faces ($N_f = 320, 1280, 5120$), $C = 1$ and $Ca = 0.5$. The standard deviations of the different shape and rheology parameters are negligible for the three meshes, whereas the errors stemming from decreasing the number of faces of the mesh are significantly small.

A.2. *Statistically stationary state and time averages*

Figure 11 depicts the time evolution of the mean deformation and relative viscosity of a suspension of capsules in the semi-dilute limit with $\phi = 0.3$ for two different values of the membrane inextensibility ($C = 1, 150$) and a fixed capillary number ($Ca = 0.5$). The time average is performed on the interval where the Taylor deformation index averaged over the number of particles reaches a steady-state value with fluctuations less than 1 %. In term of strain units, we have observed that the transient time spans over the first 5 to $7\dot{\gamma}t$.

A.3. *Grid independency*

In order to check that the system size in the periodic directions is large enough to ensure grid independency of the results, we test here the behaviour of two relevant observables, namely the mean Taylor deformation parameter, $\langle D \rangle$, and the relative viscosity, μ_r.

Box size	N_p	ϵ_D	ϵ_{μ_r}
$8r \times 8r \times 16r$	73	0.47 %	3 %
$32r \times 32r \times 16r$	1174	0.62 %	2.3 %
$64r \times 64r \times 16r$	4696	0.38 %	2 %

Table 2. Relative errors on $\langle D \rangle$ and μ_r for different system sizes.

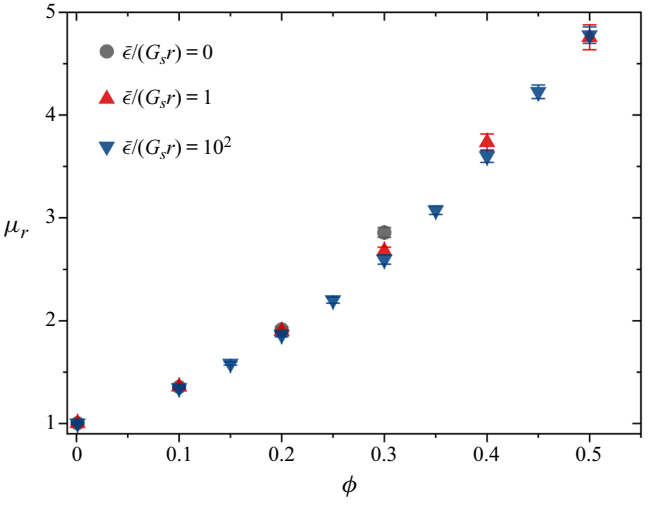

Figure 12. Effect of the short-range repulsive force on the relative viscosity of a suspension of capsules.

We performed simulations at changing the box size from $8r \times 8r \times 16r$ to $64r \times 64r \times 16r$, for fixed $C = 150$, $Ca = 0.5$, $\phi = 0.3$ and wall-to-wall distance $L = 16r$. We have varied the number of particles (N_p) to keep a fixed volume fraction. For the sake of comparison, we look at the relative (percentage) errors for the mean Taylor deformation parameter and the relative viscosity, defined as

$$\epsilon_D = \frac{\langle D \rangle - \langle D \rangle^{(0)}}{\langle D \rangle^{(0)}}, \tag{A1}$$

and

$$\epsilon_{\mu_r} = \frac{\mu_r - \mu_r^{(0)}}{\mu_r^{(0)}}, \tag{A2}$$

respectively ($\langle D \rangle^{(0)}$ and $\mu_r^{(0)}$ being the values corresponding to the cubic reference case, used throughout the paper). The results are reported in table 2. All relative errors are small and decrease from 0.47 % to 0.38 % (for the deformation parameter) and from 3 % to 2 % (for the relative viscosity), denoting a satisfactory degree of convergence for the resolution employed.

A.4. *Effect of the short-range repulsive force*

A well-known limitation of the LB-IBM scheme is the interpolation of the membrane velocity from the surrounding fluid when the distance between two boundary nodes

is below the lattice resolution limit that can result in a permanent overlap between neighbouring nodes (Krüger 2012). The probability of such event to occur increases with the volume fraction of the suspension. To prevent such situation a short-range repulsive force must be applied on neighbouring nodes from different membranes when the node-to-node distance (d_{ij}) is below one lattice spacing (Δx), whereas it vanishes for $d_{ij} > \Delta x$ (see (2.8)). Without any short-range repulsion, we do indeed observe crossing particles for $\phi > 0.3$. Such force is, therefore, needed, however its details do not affect the macroscopic behaviour of the suspension, within the range of volume fractions explored in this study. To show this, we report in figure 12 results on the relative viscosity from simulations with $C = 150$, $Ca = 0.5$ and $\phi \in [10^{-3}, 0.5]$, for three different values of the force amplitude: $\bar{\epsilon}/(G_s r) = 0$ (absence of force), $\bar{\epsilon}/(G_s r) = 1$ and $\bar{\epsilon}/(G_s r) = 10^2$ (the value used in all simulations throughout the paper). Only a slight deviation (of less than 10 %) can be detected for $\bar{\epsilon}/(G_s r) = 0$ at $\phi = 0.3$ (for larger ϕ data are not available because of the occurrence of crossings), otherwise all sets of data basically overlap, within error bars.

References

Abramowitz, M. & Stegun, I.A. 2012 *Handbook of Mathematical Functions*. Springer Science & Business Media.

Aouane, O., Xie, Q., Scagliarini, A. & Harting, J. 2018 Mesoscale simulations of Janus particles and deformable capsules in flow. In *High Performance Computing in Science and Engineering '17*, pp. 369–385. Springer.

Bagchi, P. & Kalluri, R.M. 2009 Dynamics of nonspherical capsules in shear flow. *Phys. Rev.* E **80** (1), 016307.

Bagchi, P. & Kalluri, R.M. 2010 Rheology of a dilute suspension of liquid-filled elastic capsules. *Phys. Rev.* E **81** (5), 056320.

Bagchi, P. & Kalluri, R.M. 2011 Dynamic rheology of a dilute suspension of elastic capsules: effect of capsule tank-treading, swinging and tumbling. *J. Fluid Mech.* **669**, 498–526.

Barthès-Biesel, D. 1980 Motion of a spherical microcapsule freely suspended in a linear shear flow. *J. Fluid Mech.* **100** (4), 831–853.

Barthès-Biesel, D. 2016 Motion and deformation of elastic capsules and vesicles in flow. *Ann. Rev. Fluid Mech.* **48**, 25–52.

Barthès-Biesel, D., Diaz, A. & Dhenin, E. 2002 Effect of constitutive laws for two-dimensional membranes on flow-induced capsule deformation. *J. Fluid Mech.* **460**, 211–222.

Barthès-Biesel, D. & Rallison, J.M. 1981 The time-dependent deformation of a capsule freely suspended in a linear shear flow. *J. Fluid Mech.* **113**, 251–267.

Batchelor, G.K. 1970 The stress system in a suspension of force-free particles. *J. Fluid Mech.* **41** (3), 545–570.

Batchelor, G.K. & Green, J.T. 1972 The determination of the bulk stress in a suspension of spherical particles to order C^2. *J. Fluid Mech.* **56** (3), 401–427.

Benzi, R., Succi, S. & Vergassola, M. 1992 The lattice Boltzmann equation: theory and applications. *Phys. Rep.* **222** (3), 145–197.

Bhatnagar, P.L., Gross, E.P. & Krook, M. 1954 A model for collision processes in gases. I. Small amplitude processes in charged and neutral one-component systems. *Phys. Rev.* **94** (3), 511.

Boedec, G., Leonetti, M. & Jaeger, M. 2017 Isogeometric FEM–BEM simulations of drop, capsule and vesicle dynamics in Stokes flow. *J. Comput. Phys.* **342**, 117–138.

Buxton, G.A., Verberg, R., Jasnow, D. & Balazs, A.C. 2005 Newtonian fluid meets an elastic solid: coupling lattice Boltzmann and lattice-spring models. *Phys. Rev.* E **71** (5), 056707.

Carin, M., Barthès-Biesel, D., Edwards-Lévy, F., Postel, C. & Andrei, D.C. 2003 Compression of biocompatible liquid-filled HSA-alginate capsules: determination of the membrane mechanical properties. *Biotechnol. Bioengng* **82** (2), 207–212.

Casquero, H., Bona-Casas, C., Toshniwal, D., Hughes, T.J.R., Gomez, H. & Zhang, Y.J. 2020 The divergence-conforming immersed boundary method: application to vesicle and capsule dynamics. arXiv:2001.08244.

CHANG, K.-S. & OLBRICHT, W.L. 1993*a* Experimental studies of the deformation and breakup of a synthetic capsule in steady and unsteady simple shear flow. *J. Fluid Mech.* **250**, 609–633.

CHANG, K.-S. & OLBRICHT, W.L. 1993*b* Experimental studies of the deformation of a synthetic capsule in extensional flow. *J. Fluid Mech.* **250**, 587–608.

CLAUSEN, J.R., REASOR, D.A & AIDUN, C.K. 2011 The rheology and microstructure of concentrated non-colloidal suspensions of deformable capsules. *J. Fluid Mech.* **685**, 202–234.

DE COCK, L.J., DE KOKER, S., DE GEEST, B.G., GROOTEN, J., VERVAET, C., REMON, J.P., SUKHORUKOV, G.B. & ANTIPINA, M.N. 2010 Polymeric multilayer capsules in drug delivery. *Angew. Chem. Intl Ed. Engl.* **49** (39), 6954–6973.

DODSON, W.R. & DIMITRAKOPOULOS, P. 2009 Dynamics of strain-hardening and strain-softening capsules in strong planar extensional flows via an interfacial spectral boundary element algorithm for elastic membranes. *J. Fluid Mech.* **641**, 263–296.

DODSON, W.R. III & DIMITRAKOPOULOS, P. 2010 Tank-treading of erythrocytes in strong shear flows via a nonstiff cytoskeleton-based continuum computational modeling. *Biophys. J.* **99** (9), 2906–2916.

DONBROW, M. 1991 *Microcapsules and Nanoparticles in Medicine and Pharmacy*. CRC Press.

DUPONT, C., DELAHAYE, F., BARTHÈS-BIESEL, D. & SALSAC, A.-V. 2016 Stable equilibrium configurations of an oblate capsule in simple shear flow. *J. Fluid Mech.* **791**, 738–757.

EDWARDS-LÉVY, F. & LÉVY, M.-C. 1999 Serum albumin–alginate coated beads: mechanical properties and stability. *Biomaterials* **20** (21), 2069–2084.

VON EILERS, H. 1941 Die Viskosität von Emulsionen Hochviskoser Stoffe als Funktion der Konzentration. *Kolloidn. Z.* **97** (3), 313–321.

EINSTEIN, A. 1906 Eine neue Bestimmung der Moleküldimensionen. *Ann. Phys.* **324** (2), 289–306.

EINSTEIN, A. 1911 Berichtigung zu meiner Arbeit:Eine neue Bestimmung der Moleküldimensionen. *Ann. Phys.* **339** (3), 591–592.

EVANS, K.E., NKANSAH, M.A., HUTCHINSON, I.J. & ROGERS, S.C. 1991 Molecular network design. *Nature* **353**, 124.

FARUTIN, A., BIBEN, T. & MISBAH, C. 2014 3D numerical simulations of vesicle and inextensible capsule dynamics. *J. Comput. Phys.* **275**, 539–568.

FERY, A. & WEINKAMER, R. 2007 Mechanical properties of micro- and nanocapsules: single-capsule measurements. *Polymer* **48** (25), 7221–7235.

FRANKEL, N.A. & ACRIVOS, A. 1967 On the viscosity of a concentrated suspension of solid spheres. *Chem. Engng Sci.* **22** (6), 847–853.

FRIJTERS, S., GÜNTHER, F. & HARTING, J. 2012 Effects of nanoparticles and surfactant on droplets in shear flow. *Soft Matt.* **8** (24), 6542–6556.

GALLIER, S., LEMAIRE, E., LOBRY, L. & PETERS, F. 2016 Effect of confinement in wall-bounded non-colloidal suspensions. *J. Fluid Mech.* **799**, 100–127.

GALLIER, S., LEMAIRE, E., PETERS, F. & LOBRY, L. 2014 Rheology of sheared suspensions of rough frictional particles. *J. Fluid Mech.* **757**, 514–549.

GLOWINSKI, R., PAN, T.-W., HESLA, T., JOSEPH, D.D. & PERIAUX, J. 2001 A fictitious domain approach to the direct numerical simulation of incompressible viscous flow past moving rigid bodies: application to particulate flow. *J. Comput. Phys.* **169** (2), 363–426.

GROSS, M., KRÜGER, T. & VARNIK, F. 2014 Rheology of dense suspensions of elastic capsules: normal stresses, yield stress, jamming and confinement effects. *Soft Matt.* **10** (24), 4360–4372.

GUAZZELLI, E. & POULIQUEN, O. 2018 Rheology of dense granular suspensions. *J. Fluid Mech.* **852**, P1.

GUBSPUN, J., GIRES, P.-Y., DE LOUBENS, C., BARTHES-BIESEL, D., DESCHAMPS, J., GEORGELIN, M., LEONETTI, M., LECLERC, E., EDWARDS-LÉVY, F. & SALSAC, A.-V. 2016 Characterization of the mechanical properties of cross-linked serum albumin microcapsules: effect of size and protein concentration. *Colloid Polym. Sci.* **294** (8), 1381–1389.

GUCKENBERGER, A. & GEKLE, S. 2016 A boundary integral method with volume-changing objects for ultrasound-triggered margination of microbubbles. arXiv:1608.05196.

HÄNER, E., HEIL, M. & JUEL, A. 2020 Deformation and sorting of capsules in a T-junction. *J. Fluid Mech.* **885**, A4.

HARDEMAN, M.R., GOEDHART, P.T., DOBBE, J.G.G. & LETTINGA, K.P. 1994 Laser-assisted optical rotational cell analyser (LORCA); I. A new instrument for measurement of various structural hemorheological parameters. *Clin. Hemorheol.* **14** (4), 605–618.

HECHT, M. & HARTING, J. 2010 Implementation of on-site velocity boundary conditions for D3Q19 lattice Boltzmann simulations. *J. Stat. Mech.* **2010** (01), P01018.

HOCHMUTH, R.M. 2000 Micropipette aspiration of living cells. *J. Biomech.* **33** (1), 15–22.

KOLEVA, I. & REHAGE, H. 2012 Deformation and orientation dynamics of polysiloxane microcapsules in linear shear flow. *Soft Matt.* **8** (13), 3681–3693.

KRIEGER, I.M. & DOUGHERTY, T.J. 1959 A mechanism for non-Newtonian flow in suspensions of rigid spheres. *Trans. Soc. Rheol.* **3** (1), 137–152.

KRÜGER, T. 2012 *Computer Simulation Study of Collective Phenomena in Dense Suspensions of Red Blood Cells under Shear*. Springer Science & Business Media.

KRÜGER, T., KUSUMAATMAJA, H., KUZMIN, A., SHARDT, O., SILVA, G. & VIGGEN, E.M. 2017 *The Lattice Boltzmann Method*. Springer.

KRÜGER, T., VARNIK, F. & RAABE, D. 2011 Efficient and accurate simulations of deformable particles immersed in a fluid using a combined immersed boundary lattice Boltzmann finite element method. *Comput. Maths Applics* **61** (12), 3485–3505.

LAC, E., BARTHÈS-BIESEL, D., PELEKASIS, N.A. & TSAMOPOULOS, J. 2004 Spherical capsules in three-dimensional unbounded Stokes flows: effect of the membrane constitutive law and onset of buckling. *J. Fluid Mech.* **516**, 303–334.

LÉVY, M.-C. & EDWARDS-LÉVY, F. 1996 Coating alginate beads with cross-linked biopolymers: a novel method based on a transacylation reaction. *J. Microencapsul.* **13** (2), 169–183.

LI, X. & SARKAR, K. 2008 Front tracking simulation of deformation and buckling instability of a liquid capsule enclosed by an elastic membrane. *J. Comput. Phys.* **227** (10), 4998–5018.

LOEWENBERG, M. & HINCH, E.J. 1996 Numerical simulation of a concentrated emulsion in shear flow. *J. Fluid Mech.* **321**, 395–419.

DE LOUBENS, C., DESCHAMPS, J., BOEDEC, G. & LEONETTI, M. 2015 Stretching of capsules in an elongation flow, a route to constitutive law. *J. Fluid Mech.* **767**, R3.

DE LOUBENS, C., DESCHAMPS, J., EDWARDS-LEVY, F. & LEONETTI, M. 2016 Tank-treading of microcapsules in shear flow. *J. Fluid Mech.* **789**, 750–767.

DE LOUBENS, C., DESCHAMPS, J., GEORGELIN, M., CHARRIER, A., EDWARDS-LEVY, F. & LEONETTI, M. 2014 Mechanical characterization of cross-linked serum albumin microcapsules. *Soft Matt.* **10** (25), 4561–4568.

MACMECCAN, R.M. III 2007 Mechanistic effects of erythrocytes on platelet deposition in coronary thrombosis. PhD thesis, Georgia Institute of Technology.

MARON, S.H. & PIERCE, P.E. 1956 Application of Ree–Eyring generalized flow theory to suspensions of spherical particles. *J. Colloid Sci.* **11** (1), 80–95.

MATSUNAGA, D., IMAI, Y., YAMAGUCHI, T. & ISHIKAWA, T. 2016 Rheology of a dense suspension of spherical capsules under simple shear flow. *J. Fluid Mech.* **786**, 110–127.

MITTAL, R. & IACCARINO, G. 2005 Immersed boundary methods. *Annu. Rev. Fluid Mech.* **37**, 239–261.

MIYAZAWA, K., YAJIMA, I., KANEDA, I. & YANAKI, T. 2000 Preparation of a new soft capsule for cosmetics. *J. Cosmet. Sci.* **51** (4), 239–252.

MOONEY, M. 1951 The viscosity of a concentrated suspension of spherical particles. *J. Colloid Sci.* **6** (2), 162–170.

MUELLER, S., LLEWELLIN, E.W. & MADER, H.M. 2010 The rheology of suspensions of solid particles. In *Public Relations Society of America*, vol. 466, pp. 1201–1228. The Royal Society.

MUNARIN, F., PETRINI, P., FARE, S. & TANZI, M.C. 2010 Structural properties of polysaccharide-based microcapsules for soft tissue regeneration. *J. Mater. Sci. Mater. Med.* **21** (1), 365–375.

NAVOT, Y. 1998 Elastic membranes in viscous shear flow. *Phys. Fluids* **10** (8), 1819–1833.

NEUBAUER, M.P., POEHLMANN, M. & FERY, A. 2014 Microcapsule mechanics: from stability to function. *Adv. Colloid Interface Sci.* **207**, 65–80.

PESKIN, C.S. 2002 The immersed boundary method. *Acta Numerica* **11**, 479–517.

RACHIK, M., BARTHES-BIESEL, D., CARIN, M. & EDWARDS-LEVY, F. 2006 Identification of the elastic properties of an artificial capsule membrane with the compression test: effect of thickness. *J. Colloid Interface Sci.* **301** (1), 217–226.

RAMANUJAN, S. & POZRIKIDIS, C. 1998 Deformation of liquid capsules enclosed by elastic membranes in simple shear flow: large deformations and the effect of fluid viscosities. *J. Fluid Mech.* **361**, 117–143.

ROSTI, M.E., BRANDT, L. & MITRA, D. 2018 Rheology of suspensions of viscoelastic spheres: deformability as an effective volume fraction. *Phys. Rev. Fluids* **3** (1), 012301.

SAGIS, L.M.C., DE RUITER, R., MIRANDA, F.J.R., DE RUITER, J., SCHROËN, K., VAN AELST, A.C., KIEFT, H., BOOM, R. & VAN DER LINDEN, E. 2008 Polymer microcapsules with a fiber-reinforced nanocomposite shell. *Langmuir* **24** (5), 1608–1612.

SARI, A., ALKAN, C. & KARAIPEKLI, A. 2010 Preparation, characterization and thermal properties of PMMA/n-heptadecane microcapsules as novel solid–liquid microPCM for thermal energy storage. *Appl. Energ.* **87** (5), 1529–1534.

SIEROU, A. & BRADY, J.F. 2002 Rheology and microstructure in concentrated noncolloidal suspensions. *J. Rheol.* **46** (5), 1031–1056.

SKALAK, R. 1973 Modelling the mechanical behavior of red blood cells. *Biorheology* **10** (2), 229–238.
STICKEL, J.J. & POWELL, R.L. 2005 Fluid mechanics and rheology of dense suspensions. *Annu. Rev. Fluid Mech.* **37**, 129–149.
SUCCI, S. 2001 *The Lattice Boltzmann Equation: for Fluid Dynamics and Beyond*. Oxford University Press.
SURYANARAYANA, C., RAO, K.C. & KUMAR, D. 2008 Preparation and characterization of microcapsules containing linseed oil and its use in self-healing coatings. *Prog. Org. Coat.* **63** (1), 72–78.
TAKEISHI, N., ROSTI, M.E., IMAI, Y., WADA, S. & BRANDT, L. 2019 Haemorheology in dilute, semi-dilute and dense suspensions of red blood cells. *J. Fluid Mech.* **872**, 818–848.
TAYLOR, G.I. 1934 The formation of emulsions in definable fields of flow. *Proc. R. Soc. Lond.* A **146** (858), 501–523.
VLAHOVSKA, P.M. & GRACIA, R.S. 2007 Dynamics of a viscous vesicle in linear flows. *Phys. Rev.* E **75** (1), 016313.
VLAHOVSKA, P.M., YOUNG, Y.N., DANKER, G. & MISBAH, C. 2011 Dynamics of a non-spherical microcapsule with incompressible interface in shear flow. *J. Fluid Mech.* **678**, 221–247.
WALTER, A., REHAGE, H. & LEONHARD, H. 2001 Shear induced deformation of microcapsules: shape oscillations and membrane folding. *Colloids Surf.* A **183**, 123–132.
WALTER, J., SALSAC, A.-V. & BARTHÈS-BIESEL, D. 2011 Ellipsoidal capsules in simple shear flow: prolate versus oblate initial shapes. *J. Fluid Mech.* **676**, 318–347.
WU, J. & SHU, C. 2012 Simulation of three-dimensional flows over moving objects by an improved immersed boundary–lattice Boltzmann method. *Intl J. Numer. Meth. Fluids* **68** (8), 977–1004.
ZHAO, H. & SHAQFEH, E.S.G. 2013 The dynamics of a non-dilute vesicle suspension in a simple shear flow. *J. Fluid Mech.* **725**, 709–731.